Orbits and images of cubic Galileon black holes

K. Van Aelst[1,2], E. Gourgoulhon[2], F. H. Vincent[3]

[1]Max Planck Institute for Gravitational Physics (Albert Einstein Institute), Am Mühlenberg 1, Potsdam-Golm 14476, Germany
[2]Laboratoire Univers et Théories, Observatoire de Paris, Université PSL, CNRS, Université de Paris, 5 place Jules Janssen, 92190 Meudon, France
[3]LESIA, Observatoire de Paris, Université PSL, CNRS, Sorbonne Université, Université de Paris, 5 place Jules Janssen, 92190 Meudon, France

E-mail: karim.vanaelst@aei.mpg.de, eric.gourgoulhon@obspm.fr, frederic.vincent@obspm.fr

Abstract. Null and timelike orbits are investigated in a family of hairy rotating black holes in the cubic Galileon theory. In particular, it is found that stable circular geodesics exist below a critical coupling. Their properties expectedly deviate from general relativity, which is further highlighted by computing images of an accretion disk around such black holes.

Keywords: cubic Galileon, hairy black hole, geodesics, black hole imaging

1. Introduction

Trajectories of stars and images of accretion disks orbiting black holes provide some of the main observables to test strong-field gravity [1, 2]. Such observational data are collected by complex instruments like the interferometer GRAVITY [3] and the Event Horizon Telescope (EHT) [6], which mainly focus on the supermassive black holes *Sgr A** and *M87** [4, 5, 7, 8]. The theoretical predictions for these observables have been worked out within more or less exotic frameworks: Kerr black holes (e.g. [9]), rotating black holes dressed with a complex scalar hair [10, 11], boson stars [12, 13, 14, 9], alternative black holes [15, 16, 17, 18, 19, 20, 21, 22, 23, 24], wormholes [25, 9], naked singularities [26], binary systems [27, 28]. Eventually, such analyses help constraining the nature of the observed objects [2], but also the theory within which they are modelled [29, 30].

In this spirit, the present paper examines potentially observable characteristics of black hole spacetimes within the cubic Galileon theory. The latter is the simplest of Galileons with higher order derivatives and it emerges from an effective formulation of the well-known Dvali-Gabadadze-Porrati model [31]. Explicitly, the vacuum action writes

$$S\left[g,\phi\right] = \int \left[\zeta(R-2\Lambda) - \eta(\partial\phi)^2 + \gamma(\partial\phi)^2\Box\phi\right]\sqrt{|\det g|}d^4x, \tag{1}$$

where $(\partial\phi)^2 \equiv \nabla_\mu\phi\nabla^\mu\phi$ and ζ, η and γ are coupling constants.

As a first step, the previous numerical work [32]‡ produced asymptotically flat, circular configurations of hairy rotating black holes in this theory, generalizing the non-rotating solutions obtained in [33]. A defining property of circular spacetimes is to admit a quasi-isotropic coordinate system, i.e. a coordinate system with respect to which the line element writes

$$ds^2 = -N^2dt^2 + A^2\left(dr^2 + r^2d\theta^2\right) + B^2r^2\sin^2\theta\left(d\varphi - \omega dt\right)^2. \tag{2}$$

Circular spacetimes represent a large subclass of stationary and axisymmetric spacetimes (the corresponding Killing vectors being ∂_t and ∂_ϕ), and their quasi-isotropic coordinates are well suited to study geodesics.

Regarding the Galileon field, the following ansatz is used in the numerical solutions constructed in [32]:

$$\phi = qt + \Psi(r,\theta), \tag{3}$$

where q is a nonzero constant.

In particular, the linear time-dependence is required to evade the no-scalar-hair theorem established in [34]. The latter states that, in the asymptotically flat framewok, the only static, spherically symmetric black hole metric and scalar field in the cubic Galileon theory are the Schwarzschild metric together with a trivial scalar field. However, it was shown in [33] that the non-static ansatz (3) leads to static, spherically symmetric black holes different from Schwarzschild spacetime§.

The numerical solutions constructed in [32] were rotating generalizations, and the corresponding metric expectedly deviated from Kerr spacetime. For these solutions, asymptotic flatness was imposed to evade a minimal number of assumptions of the no-hair theorem of [34]. In the cubic Galileon model (1), this notably requires $\eta = \Lambda = 0$. Then, to follow the notations of [32], the only remaining dimensionless parameter of the theory is $\bar{\gamma} = q^3 r_{\mathcal{H}}\gamma/\zeta$, where $r_{\mathcal{H}}$ is the radial coordinate of the event horizon. The present paper assesses the extent to which the metric deviations away from Kerr spacetime translate in terms of observables.

The plan of the article is as follows. Useful general results on equatorial geodesics in quasi-isotropic coordinates are summarized in section 2.1. Based on this, properties of timelike circular geodesics and photon rings (location, stability, deviation from Kerr spacetime) are studied in the static, spherically symmetric case in section 2.2, and the rotating case in section 2.3. This provides information to compute images of an accretion disk orbiting the black holes, as exposed in section 3.

‡ See this reference for more details about the motivations and limitations of the cubic Galileon model and the specific assumptions summarized below.

§ The shift-symmetry $\phi \to \phi + constant$ of action (1) is what allows a linearly time-dependent scalar field to be compatible with stationary metrics.

2. Orbits around cubic Galileon black holes

2.1. Equatorial geodesics in quasi-isotropic coordinates

The present section recalls useful results on particles freely moving in the equatorial plane of a circular spacetime, described in terms of the quasi-isotropic coordinates (2) (see [35, 36, 37] and sections 4.6 and 4.7 of [38] for closely related discussions). Based on the unique parametrization

$$\mathcal{C}: \ \lambda \mapsto (x^\mu(\lambda)) = (t(\lambda),\ r(\lambda),\ \pi/2,\ \phi(\lambda)) \tag{4}$$

such that the 4-momentum of the particle is $p^\mu = \dot{x}^\mu$ (where a dot denotes differentiation with respect to the parameter λ), the geodesic equation

$$\nabla_p p = 0 \tag{5}$$

implies that

$$E = -p_t \quad \text{is conserved along } \mathcal{C}, \tag{6}$$

$$L = p_\phi \quad \text{is conserved along } \mathcal{C}, \tag{7}$$

$$\theta = \pi/2 \quad \text{is conserved along } \mathcal{C}, \tag{8}$$

$$\frac{\dot{r}^2}{2} + \mathcal{V}(r, m, E, L) = 0, \tag{9}$$

where $m = \sqrt{-p^2}$ defines the mass of the particle, and the effective potential $\mathcal{V}$ is defined as

$$\mathcal{V}(r, m, E, L) = \frac{1}{2A^2}\left[m^2 - \left(\frac{E - \omega L}{N}\right)^2 + \left(\frac{L}{Br}\right)^2\right]. \tag{10}$$

Equation (9) is merely an explicit version of the mass conservation equation (m is conserved along $\mathcal{C}$) taking advantage of the three other conservation equations (6), (7) and (8). Thus, these four conservation equations are four necessary conditions for a curve $\mathcal{C}$ to describe an equatorial trajectory of a free particle. For non-circular orbits (i.e. $\dot{r} \neq 0$ almost everywhere), they are sufficient and have a unique solution provided that the initial sign of $\dot{r}$ is fixed and the initial coordinates $(t_0, r_0, \pi/2, \phi_0)$, the Killing energy E, the Killing angular momentum L and the mass m satisfy $\mathcal{V}(r_0, m, E, L) < 0$ and $E - \omega(r_0)L > 0$ (to guarantee that the trajectory is initially causal, i.e. future-oriented). For a circular geodesic at radial coordinate r_0, one has $\dot{r} = 0$ so that $\mathcal{V}(r_0, m, E, L) = 0$. Yet, as detailed in [37], the additional condition

$$\mathcal{V}'(r_0, m, E, L) = 0 \tag{11}$$

is required besides equations (6), (7) and (8) to realize a geodesic instead of an arbitrary (possibly accelerated) circular orbit. Rather than E and L, this constraint is usually formulated in terms of the spatial velocity V measured by the zero angular momentum observer (ZAMO)‖ as

$$\left(\frac{B'}{B} + \frac{1}{r}\right)V^2 - \frac{Br\omega'}{N}V - \frac{N'}{N} = 0. \tag{12}$$

‖ The ZAMO are characterized by a 4-velocity collinear to ∇t.

Roots exist if and only if the discriminant

$$D = \left(\frac{Br\omega'}{N}\right)^2 + \frac{4N'}{N}\left(\frac{B'}{B} + \frac{1}{r}\right) \tag{13}$$

is non-negative, in which case one has

$$V_\pm(r) = \frac{\frac{Br\omega'}{N} \pm \sqrt{D}}{2\left(\frac{B'}{B} + \frac{1}{r}\right)}. \tag{14}$$

A timelike circular geodesic (resp. photon ring) exists at r when $V_\pm$ are defined at r and at least one of them belongs to $(-1, 1)$ (resp. $\{-1, 1\}$) since the ZAMO necessarily measures a subluminal (resp. luminal) velocity. The corresponding Killing energy and angular momentum of the geodesic are

$$L_\pm = \mathcal{E} Br V_\pm, \tag{15}$$

$$E_\pm = \mathcal{E}(N + Br\omega V_\pm), \tag{16}$$

where $\mathcal{E}$ is the energy measured by the ZAMO: for a massive particle, $\mathcal{E} = \Gamma m$ where Γ is the Lorentz factor of the particle with respect to the ZAMO, while for a massless particle, $\mathcal{E} = h\nu$ where ν is the frequency measured by the ZAMO.

Finally, the radial equation (9) expectedly provides a stability criteria for circular geodesics based on convexity: for any perturbation to be bounded in some neighbourhood of a geodesic at r, $\mathcal{V}''(r, m, E, L)$ must be positive. Since the values of E and L for a circular geodesic at r are necessarily given by relations (15) and (16), one only has to study the sign of the two functions

$$\mathcal{V}''_\pm : r \mapsto \mathcal{V}''\left(r, m, E_\pm(r), L_\pm(r)\right) \tag{17}$$

on the set on which the discriminant D is non-negative. Actually, the expressions $\mathcal{V}''_\pm(r)$ are homogeneous with respect to $\mathcal{E}$, so that their sign do not depend on $\Gamma_\pm m$ in the massive case nor on $h\nu$ in the massless case. Therefore, the stability of the causal circular geodesics only depends on the sign of the two functions (17) and corresponds to massive particles where $V_\pm(r) \in (-1, 1)$ and massless ones where $V_\pm(r) = \pm 1$, regardless of whether the expressions used for $E_\pm$ and $L_\pm$ apply to a massive or a massless particle. These are therefore the two functions that are plotted in section 2 to study the stability of circular geodesics in the cubic Galileon spacetimes.

2.2. Static and spherically symmetric case

To study the geodesics of the cubic Galileon static and spherically symmetric black holes obtained in [32, 33], the procedure is to first characterize the circular geodesics. As mentioned in section 2.1, regions of positive discriminant (13) are first checked on figure 1a for different couplings ($\bar{\gamma} = 0$ corresponding to Schwarzschild spacetime). Function D appears positive everywhere down to the horizon, where it diverges because of division by the lapse N which cancels at the horizon. Therefore, circular geodesics a priori exist everywhere for all couplings, but they necessarily become superluminal near the horizon according to (14).

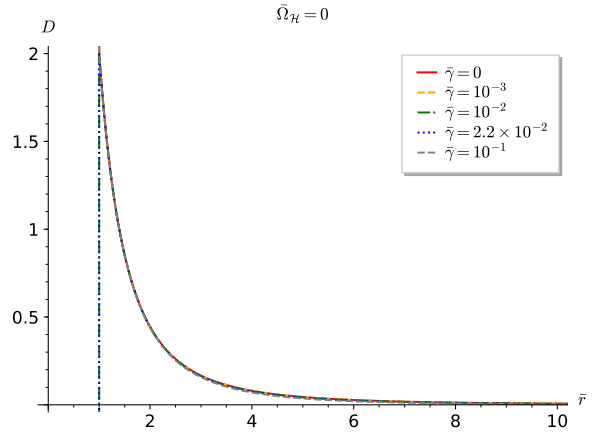

(a) Radial profile of function D whose positivity allows (possibly superluminal) circular geodesics.

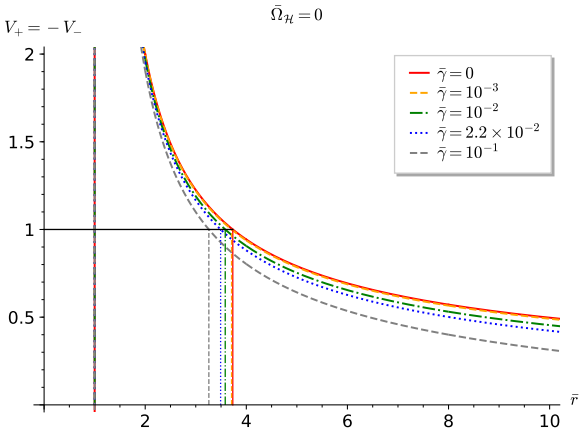

(b) Velocities and photon rings.

Figure 1: Radial profiles of D and the resulting velocities of circular geodesics in the static, spherically symmetric case (i.e. vanishing dimensionless angular velocity of the event horizon $\bar{\Omega}_{\mathcal{H}} = r_{\mathcal{H}}\Omega_{\mathcal{H}}$) for various couplings ($\bar{\gamma} = 0$ corresponding to Schwarzschild spacetime). The lapse N and its derivative are positive everywhere (see figure 2(a) of [32]), so that $D > 0$ implies that the denominator in (14) is positive. Therefore, $V_+ > 0$ (prograde orbits) and $V_- = -V_+ < 0$ (retrograde orbits).

This is what figure 1b confirms: for each coupling $\bar{\gamma}$, velocity diverges at the horizon so that there exists a photon ring (marked with a vertical line from 0 to 1), only beyond which timelike circular geodesics exist. Although D does not vary much with coupling on figure 1a, the velocities more strongly depend on $\bar{\gamma}$ because function B in the denominator does (see figure 2(b) of [32], knowing that $B = A$ everywhere in spherical symmetry). More precisely, at fixed radius, the velocity of the circular geodesic decreases with increasing coupling. As a consequence, the photon ring gets closer to the horizon as $\bar{\gamma}$ increases.

These results are related to the following facts, detailed in section 5.1 of [32]. The metric functions N and $A = B$ converge faster to Minkowski at infinity as $\bar{\gamma}$ increases. Therefore, at fixed radius away from the strong-field region, gravitation gets naively weaker as $\bar{\gamma}$ increases, so that the velocity of the circular geodesic must be smaller. In addition, for any $\bar{\gamma} \neq 0$, convergence to Minkowski spacetime is always much faster than that of Schwarzschild spacetime: N and $A = B$ converge to 1 like $1/r^4$ rather than $1/r$, yielding a vanishing Komar mass at infinity [32]. As a result, velocities given by (14) converge to zero like $r^{-\alpha/2}$ with $\alpha = 1$ in Schwarzschild spacetime and $\alpha = 4$ in Galileon spacetimes.

Such asymptotic behaviours are highlighted in figures 2. In all cases, the Lorentz factor displayed in figure 2a logically converges to 1. However, according to (15), the Killing angular momentum per unit mass $\bar{L}$ displayed in figure 2b behaves like $rV \simeq$

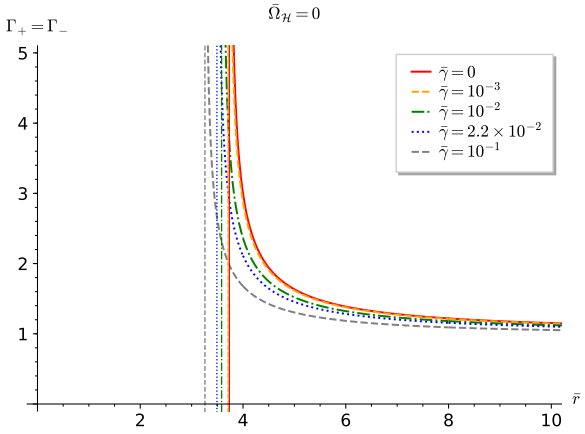

(a) Lorentz factor.

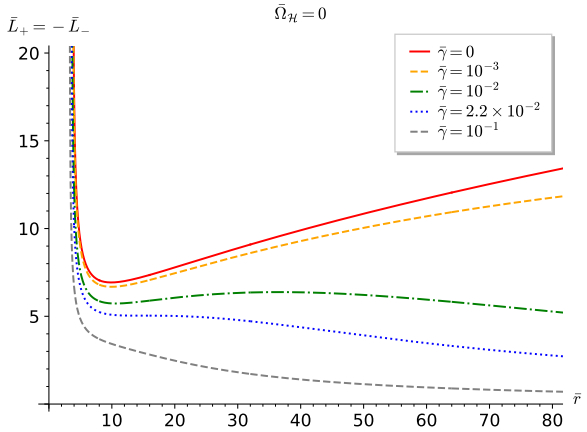

(b) Killing angular momentum.

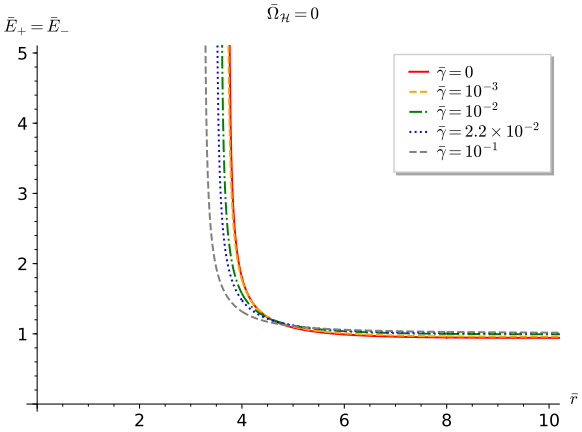

(c) Killing energy.

Figure 2: Radial profiles of kinematic quantities measured by the ZAMO for the timelike circular geodesics in the static, spherically symmetric case for various couplings. They all diverge at the photon ring (yet asymptotes are only plotted for the Lorentz factor).

$r^{1-\alpha/2}$, hence the divergence in Schwarzschild spacetime and convergence to zero for any $\bar{\gamma} \neq 0$¶. Finally, $\bar{E} = \Gamma N$ converges to 1 in all cases on figure 2c, which will hold true in the rotating case since function ω will converge to 0 like $1/r^3$ regardless of whether $\bar{\gamma}$ is zero or not. At the photon ring, all the kinematic quantities displayed in figure 2 naturally diverge.

Figure 3 assesses the stability of circular orbits for various couplings, based on the functions $\mathcal{V}''_{\pm}$ given by (17). As explained in section 2.1, its sign at a given radial coordinate r_0 is the same as $\mathcal{V}''\big(r_0, 1, \bar{E}_{\pm}(r_0), \bar{L}_{\pm}(r_0)\big)$. It appears that for any non-zero $\bar{\gamma}$, both an innermost and an outermost stable circular orbit (ISCO and OSCO) exist (they respectively correspond to the smallest and greatest r_0 such that $\mathcal{V}''_{\pm}(r_0) = 0$).

¶ The numerical solutions contain information at infinity confirming this fact even for small couplings like $\bar{\gamma} = 10^{-3}$ whose convergence to zero becomes apparent very far from the horizon.

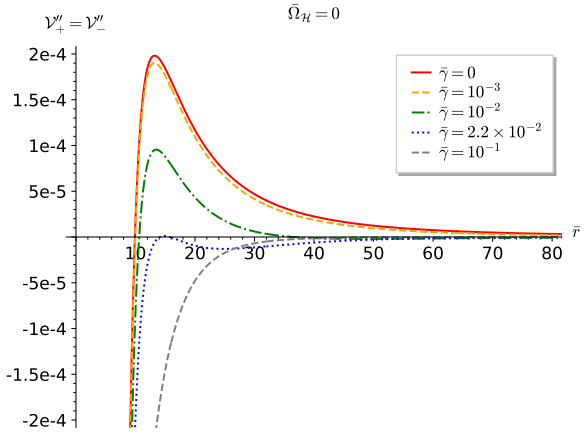

Figure 3: Radial profile of $\mathcal{V}''_{\pm}$; positivity determines stability of the geodesics.

Already, the existence of an OSCO strongly constrains the Galileon model presently studied because of the mere observation of stars orbiting in a seemingly stable way far from *Sgr A** (yet close enough for their geodesic trajectories to be ruled by *Sgr A** alone). For instance, the well-known star S2 has a non-circular orbit beyond $2500M$, where $M \simeq 4 \times 10^6 M_\odot$ is the observed mass of *Sgr A**. Although it is non-circular, such a far stable orbit indicates that a stable circular orbit should also exist somewhere between its apsides for some $\bar{E}$ and $\bar{L}$. This strongly suggests that the OSCO should be beyond the orbit of any star ruled by *Sgr A** like S2. For instance, this requires $\bar{\gamma}$ to be much smaller than 10^{-2} according to figure 3.

In addition, $\mathcal{V}''_{\pm}$ globally decreases as $\bar{\gamma}$ increases. Consequently, the ISCO radius increases while the OSCO decreases from infinity (where it is formally located in the Schwarzschild case $\bar{\gamma} = 0$). These eventually merge for a critical coupling $\bar{\gamma}^c \simeq 2.2 \times 10^{-2}$, beyond which no stable circular orbit exists anywhere. Therefore, the mere existence of stars orbiting black holes such as *Sgr A** suggests that the Galileon models presently studied are constrained to $\bar{\gamma} < \bar{\gamma}^c$ to legitimately model such static black holes. Finally, since the photon ring radius decreases (figure 1b) while the ISCO radius increases (figure 3) when $\bar{\gamma}$ increases, the photon ring always remains unstable, as it is in Schwarzschild spacetime.

2.3. Rotating case

Rotation breaks spherical symmetry so that the "+" and "-" quantities are no longer equal or opposite, as shown in figures 4 (in which solid lines correspond to the analogue quantities in Kerr spacetime). Yet all these quantities have the same behaviour at the boundaries as in the static, spherically symmetric case.

Besides, figure 4a shows that $V_+ > 0$ and $V_- < 0$ still hold everywhere. However $V_+ = -V_-$ does no longer, so that there exist a prograde photon ring and a distinct retrograde one for each angular velocity $\bar{\Omega}_{\mathcal{H}}$. As in Kerr spacetime, prograde and

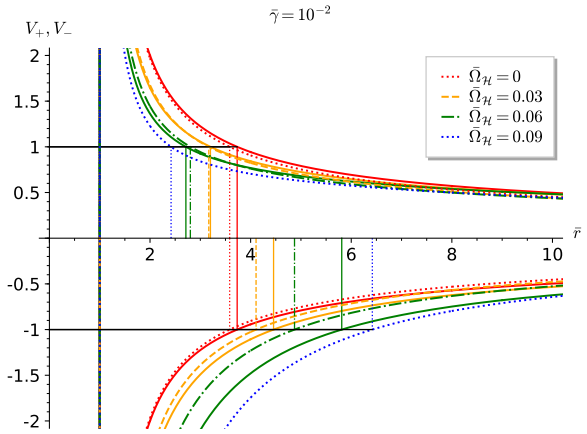

(a) Velocities ($V_+ > 0,\ V_- < 0$) and photon rings.

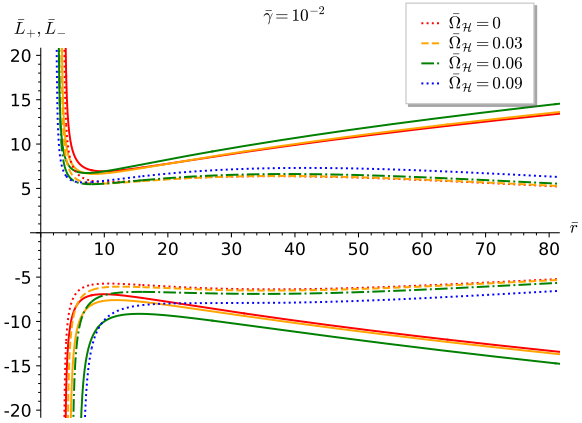

(b) Angular momentum ($\bar{L}_+ > 0,\ \bar{L}_- < 0$).

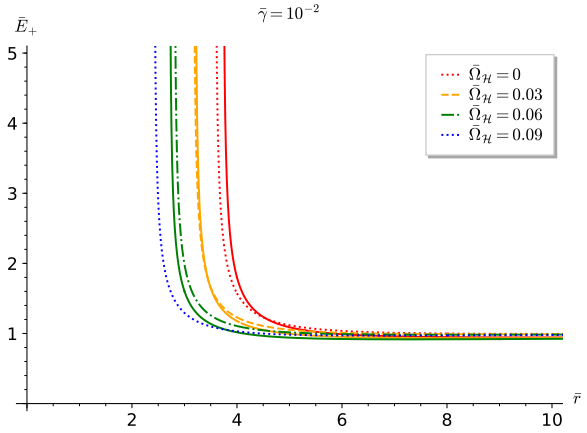

(c) Energy of prograde geodesics.

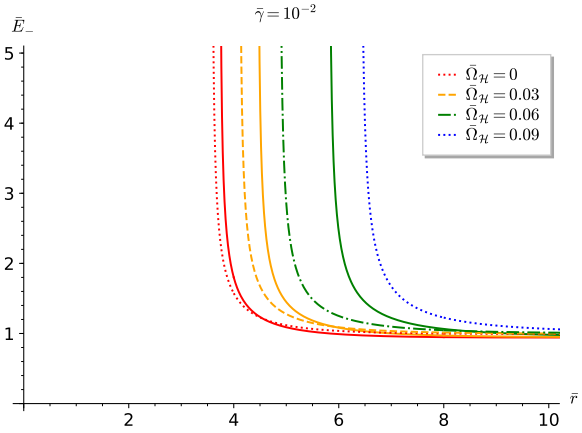

(d) Energy of retrograde geodesics.

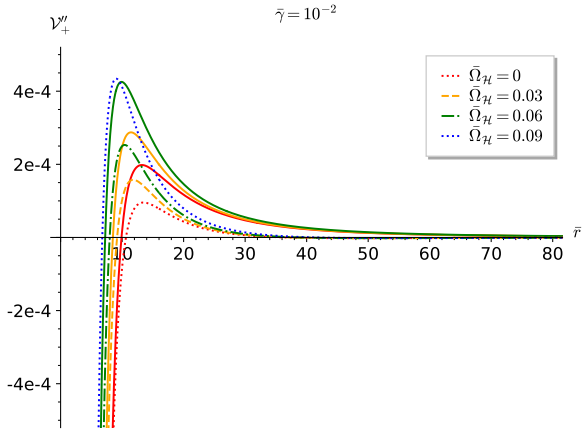

(e) Stability of prograde orbits from function $\mathcal{V}''_+$.

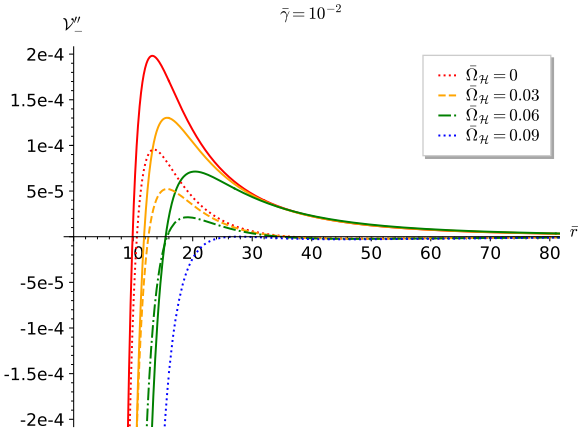

(f) Stability of retrograde orbits from function $\mathcal{V}''_-$.

Figure 4: Kinematic quantities measured by the ZAMO and stability of the timelike circular geodesics for different angular velocities $\bar{\Omega}_{\mathcal{H}}$ at fixed coupling $\bar{\gamma} = 10^{-2} < \bar{\gamma}^c$. For comparison, the profile in Kerr spacetime is plotted as a solid line with the same color for any fixed $\bar{\Omega}_{\mathcal{H}}$.

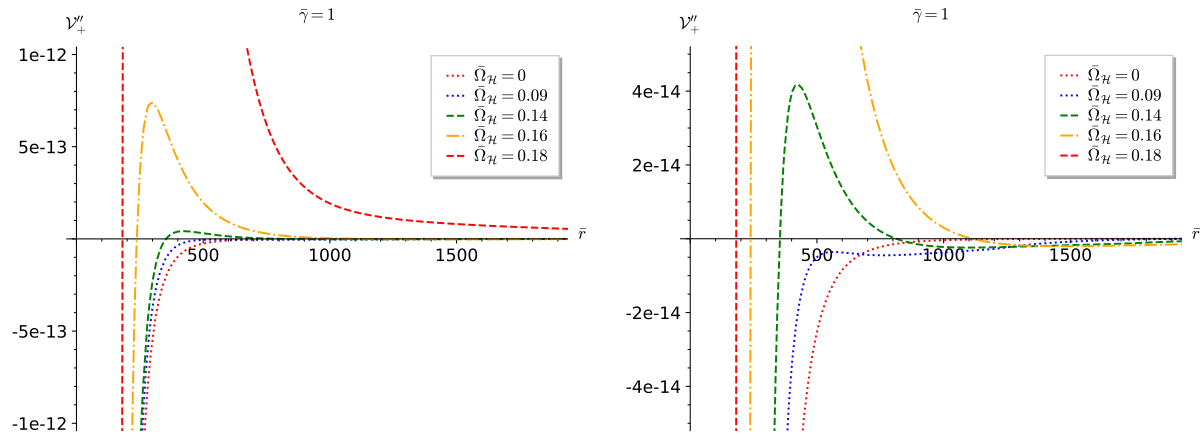

(a) Stability of prograde orbits for $\bar{\gamma} = 1 > \bar{\gamma}^c$.

(b) Zoom in figure 5a.

Figure 5: Rotation restores prograde stable orbits.

retrograde velocities decrease as $\bar{\Omega}_{\mathcal{H}}$ increases, so that the prograde (resp. retrograde) ring radius decreases (resp. increases). The dependence on $\bar{\Omega}_{\mathcal{H}}$ yet seems stronger in Kerr spacetime, meaning e.g. that the prograde ring radius decreases faster than for any nonzero $\bar{\gamma}$. Since the photon ring of the static, spherically symmetric Galileon spacetime is below that of Schwarzschild spacetime, the relative position of the Kerr and Galileon prograde rings is inverted at some $\bar{\Omega}_{\mathcal{H}}$ ($\simeq 0.03$ for $\bar{\gamma} = 10^{-2}$). On the contrary, the Kerr retrograde ring grows away from its Galileon counterpart.

The fact that the dependence on $\bar{\Omega}_{\mathcal{H}}$ is qualitatively the same in Kerr and Galileon spacetimes, but stronger in the former, also applies to $\bar{L}$ (figure 4b), $\bar{E}$ (figures 4c and 4d) and $\mathcal{V}''_{\pm}$ (figures 4e and 4f). Besides, $\mathcal{V}''_+$ (resp. $\mathcal{V}''_-$) globally increases (resp. decreases) as $\bar{\Omega}_{\mathcal{H}}$ increases; therefore, both the prograde ISCO and retrograde OSCO (resp. prograde OSCO and retrograde ISCO) radii decrease (resp. increase). Interestingly, $\mathcal{V}''_+$ may thus become positive even for $\bar{\gamma}$ greater than the critical coupling $\bar{\gamma}^c \simeq 2.2 \times 10^{-2}$ (beyond which function $\mathcal{V}''_{\pm}$ is negative everywhere in the non-rotating case) provided rotation is high enough (this is illustrated in figure 5a for $\bar{\gamma} = 1 > \bar{\gamma}^c$). Therefore, for each coupling $\bar{\gamma} > \bar{\gamma}^c$, there is a minimal angular velocitiy $\bar{\Omega}^{min}_{\mathcal{H}}(\bar{\gamma})$ beyond which stable orbits reappear, yet only prograde ones.

On the contrary, since function $\mathcal{V}''_{\pm}$ is negative everywhere for $\bar{\gamma} > \bar{\gamma}^c$ in the non-rotating case, $\mathcal{V}''_-$ gets even more negative with rotation. Therefore, the fact that stars stably orbit *Sgr A** in both directions (the spin direction of *Sgr A** is unknown) suggests that the present Galileon model is constrained to $\bar{\gamma} < \bar{\gamma}^c$ to legitimately model such rotating black holes.

As final remarks, since the ISCO radius of the static, spherically symmetric Galileon spacetime is beyond Schwarzschild's ISCO, and Kerr's retrograde ISCO increases faster with $\bar{\Omega}_{\mathcal{H}}$, the Kerr and Galileon retrograde ISCO merge at some $\bar{\Omega}_{\mathcal{H}}$ ($\simeq 0.06$ for $\bar{\gamma} = 10^{-2}$). Besides, as $\bar{\Omega}_{\mathcal{H}}$ increases further, the Galileon retrograde ISCO and

OSCO eventually merge for a critical angular velocity $\bar{\Omega}^c_{\mathcal{H}}$ ($\simeq 0.09$ for $\bar{\gamma} = 10^{-2}$), beyond which no stable retrograde orbit exists anywhere. Therefore, even for $\bar{\gamma} < \bar{\gamma}^c$, there exists a critical angular velocity $\bar{\Omega}^c_{\mathcal{H}}(\bar{\gamma})$ beyond which the Galileon solutions cannot legitimately model rotating black holes orbited by stars.

3. Images of cubic Galileon black holes

3.1. Principle of ray-tracing

In the present section, images of an accretion disk orbiting the black holes are computed numerically with the (free and open-source) ray-tracing code *GYOTO* [39]. As exposed in [40], *GYOTO* features an efficient approach to integrate the geodesic equations from the knowledge of the 3+1 quantities decomposing a numerical metric. In our case, the shift β and spatial metric γ corresponding to the quasi-isotropic metric (2) are

$$\beta = -\omega\partial_\phi, \tag{18}$$

$$\gamma = \mathrm{diag}(A^2, A^2r^2, B^2r^2\sin^2\theta). \tag{19}$$

Images are computed in the following way. An explicit model of accretion flow is set around the black hole[+]. A telescope set in the numerical metric mimicks the observing wavelength (1.3 mm), the distance (16.9 Mpc), field of view (120 μas) and orientation of the Event Horizon Telescope with respect to *M87** (the black hole being set at the origin and the disk lying in the equatorial plane $\theta = 90°$, the colatitude of the Earth is $\theta = 160°$, while the vertical axis of the screen of the EHT is rotated by 110° clockwise from the projection on the screen of the spin axis of the disk). Each pixel of its focal screen corresponds to a spatial direction, which uniquely defines the initial tangent vector of a null affinely parametrized geodesic. The latter is integrated backwards in time until a stopping condition is met, e.g. the photon gets too close to the event horizon, or definitely leaves the strong field region. Otherwise, every time the geodesic crosses the accretion disk, the radiative transfer equations ruling the specific intensity are integrated along the segment lying within the disk. The cumulated specific intensity is eventually plotted on the initial pixel.

Yet, determining the nature and properties of a compact object based on the image of its accretion flow is a very degenerate inverse problem [19, 26, 41]. This is for instance evidenced in reference [13] in which the same model of accretion disk is set around a boson star and a black hole: the deviations between the resulting images are very subtle although the natures of the accreting objects are very different. Furthermore, the resolution of present and future instruments like the EHT is limited, making it even harder to distinguish subtle features[*].

[+] Rough estimates, confirmed by simple exact models of accretion disks, show that the gravitational influence of an accretion disk is usually completely negligible with respect to the black hole. Thus, the vacuum black hole metrics are still valid in presence of an accretion disk. See section 6.5 of [1] for quantitative arguments.

[*] Regarding the particular problem of distinguishing boson stars from black holes, see however [14]

Then, the purpose of numerical images is not systematically to check whether the image constructed by the EHT [8] can be reproduced for different accreting compact objects. This indeed requires costly GRMHD simulations, together with a model of the EHT itself. Instead, strong efforts are made to propose fairly simple and yet realistic models of accretion disks [42, 43, 44, 9]. In particular, such models are assumed to be good approximations of stable steady solutions of the GRMHD equations. Comparing the resulting images for different compact objects provides a more efficient and still relevant method to evaluate how degenerate the problem is. The hope is that such an approach should help isolating the causes of differences between images, e.g. being able to guess the nature and amplitudes of the modifications that result from changing the accretion model or the theory used to describe the whole system.

As a result, a simple model of accretion disk, recently introduced in [9], is used in the sections below. Like *Sgr A**, supermassive black hole *M87** features a very low-luminosity accretion flow, revealing an inefficient radiative cooling and hence a high temperature. It is consistently modelled as a low accretion rate, geometrically thick, optically thin disk♯ [45]. Besides these properties, only the thermal synchrotron emission is computed, following a method exposed in [46]. In the end, the complete model is described by very few input parameters: the opening angle and inner edge of the disk (which is set at the ISCO in our case), the magnetization parameter (which determines the ambient magnetic field strength), the electron density and temperature at the inner edge (which determine the density and temperature profiles).

3.2. Static and spherically symmetric case

To connect with section 2, the black holes on figure 6 all have the same radius, namely the Schwarzschild radius of *M87** (in quasi-isotropic coordinates, i.e. $r_{\mathcal{H}} = M_{M87^*}/2$ where $M_{M87^*} \simeq 6.5 \times 10^9 M_\odot$). It is actually more natural to manipulate the horizon radius than any notion of mass: because of the non-Schwarzschild asymptotics of the Galileon black holes recalled in section 2.2, there is no relevant mass parameter that can be extracted from star trajectories (through Kepler's law) or surface integrals (such as the Komar or ADM masses) in the weak field region, since its value could not be compared in any meaningful way to that of a Schwarzschild black hole (recall for instance that these Galileon black holes feature a vanishing Komar mass at spatial infinity, and yet admit stable orbits). It is thus equally legitimate to make comparisons based on parameters specific to the strong field region such as the horizon, lightring and ISCO radii, and the characteristics of the images described below.

In the non-rotating case, images 6a and 6b compare the Schwarzschild limit $\bar{\gamma} = 0$ to a static and spherically symmetric Galileon black hole below the critical coupling. In both cases, the ISCO radius is read from figure 3. The asymmetries within each

for possibly detectable deviations arising from dynamical effects revealed by 3D general relativistic magnetohydrodynamics simulations.

♯ An accretion disk is geometrically (resp. optically) thin when the opening angle (resp. optical depth) is smaller than 1. It is geometrically (resp. optically) thick otherwise.

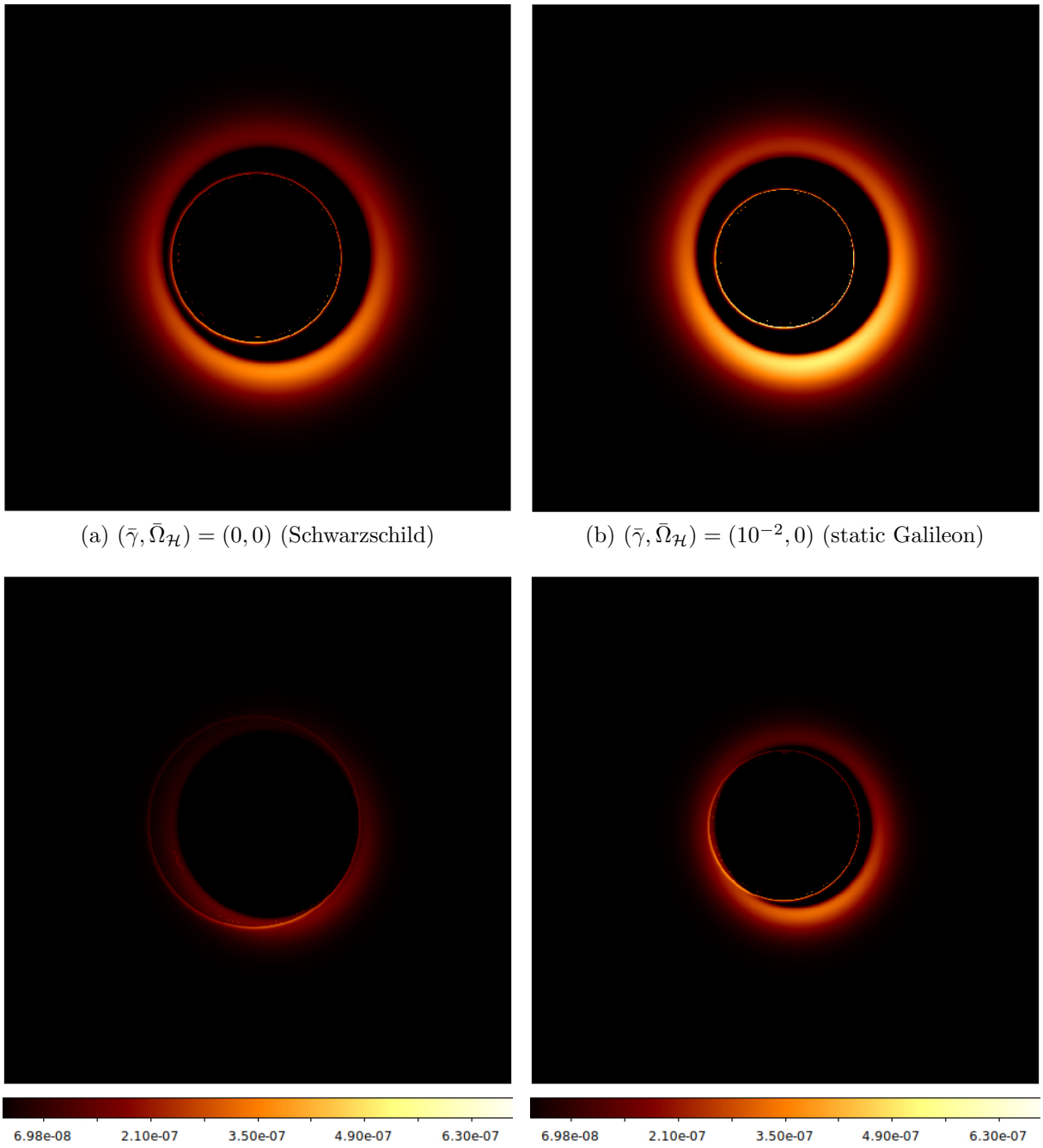

(a) $(\bar{\gamma}, \bar{\Omega}_{\mathcal{H}}) = (0, 0)$ (Schwarzschild)

(b) $(\bar{\gamma}, \bar{\Omega}_{\mathcal{H}}) = (10^{-2}, 0)$ (static Galileon)

(c) $(\bar{\gamma}, \bar{\Omega}_{\mathcal{H}}) = (0, 0.07)$ (Kerr)

(d) $(\bar{\gamma}, \bar{\Omega}_{\mathcal{H}}) = (10^{-2}, 0.07)$ (rotating Galileon)

Figure 6: Images at 1.3 mm produced by a thick accretion disk orbiting black holes for various couplings $\bar{\gamma}$ and angular velocity $\bar{\Omega}_{\mathcal{H}}$ (fixed horizon radius $r_{\mathcal{H}} = M_{M87^*}/2$). The field of view equals $120\,\mu$as. The linear scale of the specific intensity I_ν is provided in SI units ($I_\nu = 4 \times 10^7$ SI corresponds to a brightness temperature $\sim 25 \times 10^9$ K).

image come from the configuration of the EHT with respect to the accretion disk. More precisely, the 110° clockwise rotation of the vertical axis of the screen from the projected spin axis of the disk explains the position on the images of the brighter spot that results from the relativistic beaming and blueshift affecting the part of the disk rotating towards the screen. Besides, the inside luminous ring corresponds to the secondary and higher order images, which aymptotically accumulate in the direction of the lightring. Rather than being centered within the primary image of the disk, this ring appears shifted towards the top of the spin axis because of the inclination angle $\theta = 160°$ of the EHT observer (the disk is almost seen from below).

This ring gets smaller with respect to the primary image as $\bar{\gamma}$ increases because the ISCO radius increases (figure 3) while the lightring decreases (figure 1b). Explicitly, in Schwarzschild case, the internal diameter of the primary image is $D \simeq 50\,\mu$as while the diameter of the secondary ring is $d \simeq 42\,\mu$as, which is compatible with the EHT image [8]. In the Galileon case, $D \simeq 46\,\mu$as while $d \simeq 34\,\mu$as. Besides, the image is globally brighter as $\bar{\gamma}$ increases. This is consistent with the fact that asymptotic convergence to Minkowski is faster as $\bar{\gamma}$ increases (as recalled in section 2.2). In other terms, the strong field region shrinks as $\bar{\gamma}$ increases, so that most light rays undergo a weaker gravitational redshift.

Therefore, if one considered a Galileon black hole with e.g. a 1.12 times greater radius, so as to fit the internal and secondary diameters close enough to the Schwarzschild values (the deviation on their ratio being possibly undetectable by the resolution of the EHT††), the corresponding image would get even brighter than figure 6b. One could accordingly reduce the density parameter to avoid tension with the observed luminosity. Yet the fact would remain that the ISCO radius would be even greater than it already is with respect to its Schwarzschild analogue when the horizon radii are the same (figure 3). It is hardly conceivable that the ISCO radius of *M87** could be estimated by other means than EHT-type observations, so that no incompatiblity related to this parameter could be exhibited. On the other hand, if images of *Sgr A** were obtained, tensions about the ISCO location should arise based on the high precision astrometric observations made by the instrument GRAVITY which detected "flares" [5] close to Schwarzschild ISCO, knowing that such bright spots are expected to materialize near the inner edge of the accretion disk of *Sgr A**.

3.3. Rotating case

Images 6c and 6d compare a Kerr black hole to a rotating Galileon black hole sharing the same angular velocity. In both cases, the inner edge of the disk is set at the prograde ISCO, which is read from figure 4e. Besides, the inside ring intersects the primary image,

†† Actually, in order to reproduce even more closely the diameters, and hence their ratio, one could fine tune the dimension of the internal diameter of the primary image by considering a more realistic scenario involving accreting matter on non circular trajectories below the ISCO. In this sense, the secondary ring is more reliable as an observable of the gravitational field as it weakly depends on the boundaries and physical properties of the accretion process.

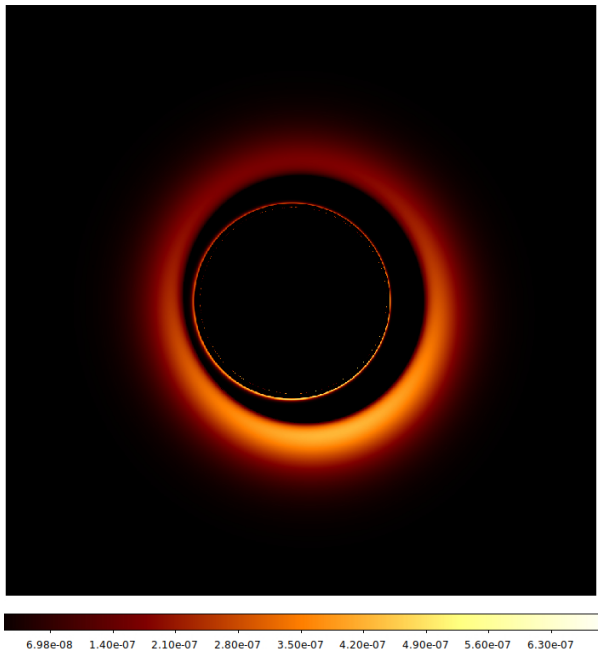

Figure 7: Case $(\bar{\gamma}, \bar{\Omega}_{\mathcal{H}}) = (10^{-2}, 0.03)$ such that $r_{\mathcal{H}} = 1.2M_{M87*}/2$. To compare with figure 6a.

meaning that the ISCO is close enough to the light ring to allow photons to cross the disk at least a second time. This is consistent with the fact that the prograde ISCO decreases (figure 4e) faster than the prograde lightring (figure 4a) as $\bar{\Omega}_{\mathcal{H}}$ increases. As in the static case, the image is globally brighter as $\bar{\gamma}$ increases. But at a fixed $\bar{\gamma}$, the images get darker as $\bar{\Omega}_{\mathcal{H}}$ increases because the strong field region expectedly expands with rotation.

As illustrated by figure 7, such tendencies leave room for a black hole with moderately low rotation, and radius greater than $M_{M87*}/2$, to closely mimick Schwarzschild image 6a in terms of dimensions and brightness. Yet regarding the ISCO radius, the fit is expectedly not so good with respect to Schwarzschild (9% and 50% deviation on the prograde and retrograde ISCO respectively). Of course, clearing away degenerate tendencies and exhibiting significant incompatibilities would only be possible if images and more precise spin measurements of *Sgr A** were available.

4. Conclusion

Investigating the geodesics of the cubic Galileon black holes constructed in [32] exhibits non viable characteristics. The presence of an OSCO constrains the coupling $\bar{\gamma}$ to smaller and smaller values as stars are detected orbiting black holes farther and farther, such as S2 around *Sgr A**. Such constraint also arises from the image of a disk accreting onto the black holes: as $\bar{\gamma}$ increases, the global brightness and relatives dimensions of the luminous structures deviate from the general relativity analogues. This can possibly be

compensated by adjusting density, rotation and the horizon radius, but then significant deviations arise in regards of the ISCO radius.

These qualitative comparisons are not free of simplifications (both in the metric and the model of disk), which could be addressed in later work. As explained in [32], the circular metric (2) is only exact in the static case, because cubic Galileon black holes coupled to the scalar ansatz (3) actually become noncircular for nonzero $\bar{\Omega}_{\mathcal{H}}$. Reproducing the rotating solutions in a noncircular framework would allow to reach accurate rapidly rotating solutions (possibly up to an extremal case). Such accurate framework would also be used to construct asymptotically de Sitter configurations, whose deviations from general relativity are naively expected to be less significant than the present asymptotically flat configurations, because no coefficient in the asymptotic expansion in $1/r$ should vanish in the static limit [33]. Furthermore, to make precise quantitative comparisons between actual images and numerical predictions in a consistent way, more realistic models of disk such as ion tori could be considered (these are geometrically thick and optically thin structures too, yet featuring more complex density and temperature profiles derived from first principles, as well as isotropic [42] or toroidal [44] magnetic fields).

Acknowledgements

KV and EG acknowledge support from the CNRS program 80PRIME-TNENGRAV.

References

[1] Bambi C 2017 *Black Holes: A Laboratory for Testing Strong Gravity* (Springer) ISBN 978-981-10-4524-0

[2] Cardoso V and Pani P 2019 *Living Rev. Rel.* **22** 4 ISSN 1433-8351 URL https://doi.org/10.1007/s41114-019-0020-4

[3] Abuter R *et al.* 2017 *A&A* **602** A94 URL https://doi.org/10.1051/0004-6361/201730838

[4] GRAVITY Collaboration 2018 *A&A* **615** L15 URL https://doi.org/10.1051/0004-6361/201833718

[5] GRAVITY Collaboration 2018 *A&A* **618** L10 URL https://doi.org/10.1051/0004-6361/201834294

[6] Doeleman S *et al.* 2009 *ASTRO2010 Decadal Review Panels* (*Preprint* 0906.3899)

[7] Issaoun S *et al.* 2019 *ApJ* **871** 30 URL https://iopscience.iop.org/article/10.3847/1538-4357/aaf732

[8] Collaboration T E *et al.* 2019 *ApJL* **875** 1 URL https://iopscience.iop.org/article/10.3847/2041-8213/ab0ec7

[9] Vincent F H, Wielgus M, Abramowicz M A, Gourgoulhon E, Lasota J P, Paumard T and Perrin G 2021 *Astron. Astrophys.* **646** A37 (*Preprint* 2002.09226) URL https://doi.org/10.1051/0004-6361/202037787

[10] Vincent F H, Gourgoulhon E, Herdeiro C and Radu E 2016 *Phys. Rev. D* **94** 084045 URL https://link.aps.org/doi/10.1103/PhysRevD.94.084045

[11] Collodel L G, Doneva D D and Yazadjiev S S 2021 (*Preprint* 2101.05073)

[12] Grould M, Meliani Z, Vincent F H, Grandclément P and Gourgoulhon E 2017 *Class. Quantum Gravity* **34** 215007 URL https://doi.org/10.1088/1361-6382/aa8d39

[13] Vincent F H, Meliani Z, Grandclément P, Gourgoulhon E and Straub O 2016 *Class. Quantum Gravity* **33** 105015 URL https://doi.org/10.1088%2F0264-9381%2F33%2F10%2F105015
[14] Olivares H, Younsi Z, Fromm C M, De Laurentis M, Porth O, Mizuno Y, Falcke H, Kramer M and Rezzolla L 2020 *Mon. Not. Roy. Astron. Soc.* **497** 521–535 ISSN 0035-8711 (*Preprint* https://academic.oup.com/mnras/article-pdf/497/1/521/33528097/staa1878.pdf) URL https://doi.org/10.1093/mnras/staa1878
[15] Vetsov T, Gyulchev G and Yazadjiev S 2018 (*Preprint* 1801.04592)
[16] Wang M, Chen S and Jing J 2017 *J. Cosmol. Astropart. Phys.* **2017** 051–051 URL https://doi.org/10.1088/1475-7516/2017/10/051
[17] Tsukamoto N 2018 *Phys. Rev. D* **97**(6) 064021 URL https://link.aps.org/doi/10.1103/PhysRevD.97.064021
[18] Wang H M, Xu Y M and Wei S W 2019 *J. Cosmol. Astropart. Phys.* **2019** 046–046 URL https://doi.org/10.1088/1475-7516/2019/03/046
[19] Abdikamalov A B, Abdujabbarov A A, Ayzenberg D, Malafarina D, Bambi C and Ahmedov B 2019 *Phys. Rev. D* **100**(2) 024014 URL https://link.aps.org/doi/10.1103/PhysRevD.100.024014
[20] Moffat J W and Toth V T 2020 *Phys. Rev. D* **101**(2) 024014 URL https://link.aps.org/doi/10.1103/PhysRevD.101.024014
[21] Khodadi M, Allahyari A, Vagnozzi S and Mota D F 2020 *J. Cosmol. Astropart. Phys.* **2020** 026–026 URL https://doi.org/10.1088/1475-7516/2020/09/026
[22] Das A, Saha A and Gangopadhyay S 2020 *Eur. Phys. J. C* **80** 180 ISSN 1434-6052 URL https://doi.org/10.1140/epjc/s10052-020-7726-z
[23] Wei S W and Liu Y X 2020 (*Preprint* 2003.07769)
[24] Guo M and Li P C 2020 *Eur. Phys. J. C* **80** 588 ISSN 1434-6052 URL https://doi.org/10.1140/epjc/s10052-020-8164-7
[25] Lamy F, Gourgoulhon E, Paumard T and Vincent F H 2018 *Class. Quantum Gravity* **35** 115009 URL https://doi.org/10.1088%2F1361-6382%2Faabd97
[26] Shaikh R and Joshi P S 2019 *J. Cosmol. Astropart. Phys.* **2019** 064–064 URL https://doi.org/10.1088/1475-7516/2019/10/064
[27] Cunha P V P, Herdeiro C A R and Rodriguez M J 2018 *Phys. Rev. D* **97**(8) 084020 URL https://link.aps.org/doi/10.1103/PhysRevD.97.084020
[28] Cunha P V P, Herdeiro C A R and Rodriguez M J 2018 *Phys. Rev. D* **98**(4) 044053 URL https://link.aps.org/doi/10.1103/PhysRevD.98.044053
[29] Psaltis D *et al.* (EHT Collaboration) 2020 *Phys. Rev. Lett.* **125**(14) 141104 URL https://link.aps.org/doi/10.1103/PhysRevLett.125.141104
[30] Völkel S, Barausse E, Franchini N and Broderick A E 2020 (*Preprint* 2011.06812)
[31] Dvali G, Gabadadze G and Porrati M 2000 *Phys. Lett. B* **485** 208–214
[32] Van Aelst K, Gourgoulhon E, Grandclément P and Charmousis C 2020 *Class. Quantum Gravity* **37** 035007 URL https://doi.org/10.1088%2F1361-6382%2Fab6391
[33] Babichev E, Charmousis C, Lehébel A and Moskalets T 2016 *J. Cosmol. Astropart. Phys.* **1609** 011 (*Preprint* 1605.07438) URL https://doi.org/10.1088%2F1475-7516%2F2016%2F09%2F011
[34] Hui L and Nicolis A 2013 *Phys. Rev. Lett.* **110** 241104 (*Preprint* 1202.1296) URL https://link.aps.org/doi/10.1103/PhysRevLett.110.241104
[35] Bardeen J 1970 *ApJ* **161** 103–9
[36] Bardeen J, Press W and Teukolsky S 1972 *ApJ* **178** 347
[37] Van Aelst K 2020 *Class. Quantum Gravity* **37** 207001 URL https://doi.org/10.1088/1361-6382/aba80c
[38] Gourgoulhon E 2010 An introduction to the theory of rotating relativistic stars *CompStar 2010: School and Workshop on Computational Tools for Compact Star Astrophysics Ganil, Caen, France, February 8-16, 2010* (*Preprint* 1003.5015)
[39] Vincent F H, Paumard T, Gourgoulhon E and Perrin G 2011 *Class. Quantum Gravity* **28** 225011

URL https://doi.org/10.1088%2F0264-9381%2F28%2F22%2F225011
[40] Vincent F H, Gourgoulhon E and Novak J 2012 *Class. Quantum Gravity* **29** 245005 URL https://doi.org/10.1088%2F0264-9381%2F29%2F24%2F245005
[41] Glampedakis K and Pappas G 2021 (*Preprint* 2102.13573)
[42] Straub, O, Vincent, F H, Abramowicz, M A, Gourgoulhon, E and Paumard, T 2012 *A&A* **543** A83 URL https://doi.org/10.1051/0004-6361/201219209
[43] Abramowicz M A and Fragile P C 2013 *Living Rev. Relativ.* **16** 1 ISSN 1433-8351 URL https://doi.org/10.12942/lrr-2013-1
[44] Vincent, F H, Yan, W, Straub, O, Zdziarski, A A and Abramowicz, M A 2015 *A&A* **574** A48 URL https://doi.org/10.1051/0004-6361/201424306
[45] Yuan F and Narayan R 2014 *Annu. Rev. Astron. Astrophys.* **52** 529–588 (*Preprint* https://doi.org/10.1146/annurev-astro-082812-141003) URL https://doi.org/10.1146/annurev-astro-082812-141003
[46] Pandya A, Zhang Z, Chandra M and Gammie C F 2016 *ApJ* **822** 34 URL https://doi.org/10.3847%2F0004-637x%2F822%2F1%2F34